Energy Materials and Devices

Open Access
Research Article

Graphical Abstract

Dual-functional hydrazide–indole additive for boosting efficiency and stability in perovskite solar cells

Zhuo Peng[1,#,†], Han Wang[1,†], Jiazhi Meng[1], Xin Hong[1], Kefei Shi[2], Wenqiang Ding[1], Jianghao Yin[1], Na Liu[3], Chengcheng Wu[1] ✉, Guodan Wei[1] ✉, and Feiyu Kang[1]

[1] *Institute of Materials Science, Tsinghua Shenzhen International Graduate School, Tsinghua University, Shenzhen 518000, China*
[2] *Department of Materials Science and Engineering, University of Illinois at Urbana-Champaign, Urbana, IL 61801, USA*
[3] *Faculty of Materials Science MSU-BIT University, Shenzhen 518172, China*
[#] *Current affiliation: State Key Laboratory of Space Information System and Integrated Application, Beijing Institute of Satellite Information Engineering, Beijing 100086, China*

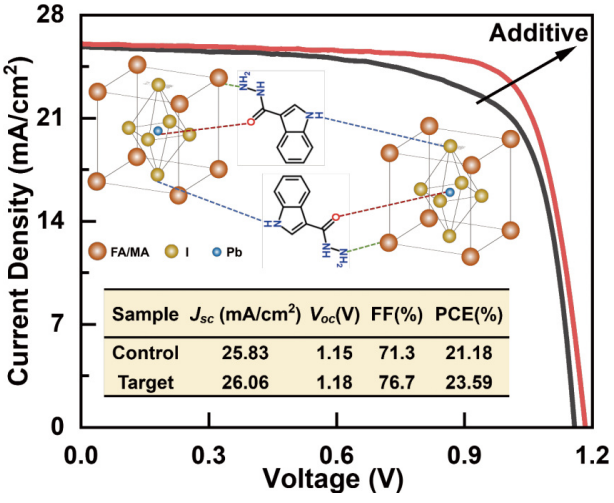

The incorporation of 1H-indole-3-carbohydrazide (1H-CBH) as a multifunctional additive enables synergistic defect passivation in perovskite solar cells through dual coordination with uncoordinated Pb^{2+} ions and hydrogen bonding with uncoordinated I^-/FA^+ species. This strategy suppresses nonradiative recombination, enhances charge transport, and improves the interfacial compatibility, achieving a power conversion efficiency of 23.59% in mixed-cation perovskite solar cells. The modified devices also exhibit exceptional stability, retaining 80% of their initial power conversion efficiency after 600 h under an inert N_2 atmosphere, with preservation of their morphology for 8 months under ambient conditions.

✉ Address correspondence to
Guodan Wei,
weiguodan@sz.tsinghua.edu.cn;
Chengcheng Wu,
wucc@tsinghua.edu.cn

Received: December 12, 2025
Revised: January 6, 2026
Accepted: January 14, 2026

Read Online

Citation: Peng Z., Wang H., Meng J., et al. Dual-functional hydrazide–indole additive for boosting efficiency and stability in perovskite solar cells. *Energy Mater. Devices*, 2026, 4(1), 9370088. https://doi.org/10.26599/EMD.2026.9370088

Energy Materials and Devices
https://doi.org/10.26599/EMD.2026.9370088
Open Access
Research Article

Dual-functional hydrazide–indole additive for boosting efficiency and stability in perovskite solar cells

Zhuo Peng[1,#,†], Han Wang[1,†], Jiazhi Meng[1], Xin Hong[1], Kefei Shi[2], Wenqiang Ding[1], Jianghao Yin[1], Na Liu[3], Chengcheng Wu[1] ✉, Guodan Wei[1] ✉, and Feiyu Kang[1]

[1] *Institute of Materials Science, Tsinghua Shenzhen International Graduate School, Tsinghua University, Shenzhen 518000, China*
[2] *Department of Materials Science and Engineering, University of Illinois at Urbana-Champaign, Urbana, IL 61801, USA*
[3] *Faculty of Materials Science MSU-BIT University, Shenzhen 518172, China*
[#] *Current affiliation: State Key Laboratory of Space Information System and Integrated Application, Beijing Institute of Satellite Information Engineering, Beijing 100086, China*
[†] *Zhuo Peng and Han Wang contributed equally to this work.*

Cite this article: *Energy Mater. Devices* 2026, **4**(1): 9370088. https://doi.org/10.26599/EMD.2026.9370088

ABSTRACT

Perovskite solar cells (PSCs) have attracted considerable attention as next-generation photovoltaic technologies owing to their solution processability, low weight, and mechanical flexibility. Despite rapid progress, defect-induced nonradiative recombination remains a major obstacle, hindering further improvements in the device efficiency and operational stability. In this study, we introduce 1H-indole-3-carbohydrazide (1H-CBH) as a multifunctional molecular additive that effectively mitigates these issues through synergistic defect passivation. Specifically, 1H-CBH simultaneously coordinates with uncoordinated Pb^{2+} ions and forms hydrogen bonds with uncoordinated I^- ions and formamidinium cations. This dual interaction strategy promotes the growth of larger grains, reduces the density of grain boundary defects, and enhances the interfacial compatibility with the electron-transport layer, thereby enabling improved charge transport. Consequently, the incorporation of 1H-CBH into mixed-cation PSCs yields a remarkable enhancement in the power conversion efficiency from 21.18% to 23.59%. Moreover, the 1H-CBH-modified devices demonstrated exceptional environmental stability, retaining their initial morphology after 8 months under ambient conditions (25°C, 50%–80% relative humidity), whereas their unpassivated counterparts underwent complete degradation. Under inert N_2 atmosphere, PSCs incorporating 1H-CBH maintained >80% of their initial power conversion efficiency after 600 h continuous storage. These results highlight the critical role of multifunctional additive engineering in achieving highly efficient and durable perovskite solar cells, paving the way toward scalable and reliable photovoltaic technologies.

KEYWORDS

perovskite solar cell, additive engineering, defect passivation, power conversion efficiency, stability enhancement

1 Introduction

Perovskite solar cells (PSCs) have rapidly emerged as a leading next-generation photovoltaic technology owing to their outstanding solution processability, low weight, and mechanical flexibility. These unique advantages not only enable the seamless integration of PSCs into visible and functional surfaces, including building facades, vehicles, and consumer electronics, but also support their deployment across diverse application domains such as indoor photovoltaics, Internet of Things devices, and residential energy systems[1–4]. Recently, a certified power conversion efficiency (PCE) of 27% was achieved by the Soochow/UNSW/BaimaLake collaboration[5], setting a new benchmark on the National Renewable Energy Laboratory (NREL) chart, with an open-circuit voltage (V_{oc}) of 1.20 V, short-circuit current density (J_{sc}) of 26.34 mA cm^{-2}, and fill factor (FF) of 85.4%. Despite these significant advancements, the performance of existing PSCs still falls short of the Shockley–Queisser (S–Q) limit of 30.14% for an ideal 1.6 eV bandgap[6]. Bridging this efficiency gap is essential for realizing the full photovoltaic potential of perovskite materials and pushing the efficiency beyond 27%[7–10]. For example, a record V_{oc} of 1.255 V was achieved in wide-bandgap (1.67 eV) perovskites through nucleation and crystallization control using mixed, green antisolvents, approaching the S–Q limit V_{oc} of 1.309 V[11]. Among the remaining challenges, defect-induced nonradiative recombination represents a major bottleneck that severely limits further improvements in the efficiency. Defects within the bulk and interfacial regions of perovskites create trap states that act as nonradiative recombination centers,

Received: December 12, 2025 / **Revised:** January 6, 2026 / **Accepted:** January 14, 2026

✉ **Address correspondence to** Guodan Wei, weiguodan@sz.tsinghua.edu.cn; Chengcheng Wu, wucc@tsinghua.edu.cn

resulting in V_{oc} losses and an overall lower PCE[12–17]. Compared to single-crystal perovskites, polycrystalline thin films prepared via scalable deposition techniques typically exhibit a higher trap density, further exacerbating recombination losses[18,19]. Both shallow traps originating from intrinsic point defects and deep traps associated with surface or grain boundary imperfections contribute to the degradation of the V_{oc} and FF, thereby compromising the efficiency and stability of devices[20,21]. Furthermore, nonradiative recombination reduces quasi-Fermi level splitting (QFLS), causing charge-carrier losses and inherent V_{oc} deficits[22–24]. Therefore, suppressing defect-mediated recombination through effective defect passivation strategies is essential for pushing the performance of PSCs toward the theoretical limit[25–28].

To address these issues, additive engineering by introducing functional molecules into the formulations of perovskite precursors has emerged as one of the most effective strategies for mitigating voltage losses and enhancing the V_{oc} [29–32]. Common defect sources, including the evaporation of A-site cations, presence of uncoordinated Pb^{2+}/Pb^{0} clusters, and halide-ion migration, often compromise the long-term stability of PSCs[33–36]. Conventional solvent additives, such as dimethyl sulfoxide (DMSO) and *N*-methyl-2-pyrrolidone (NMP), can temporarily coordinate with PbI_2 to modulate its crystallization; however, these solvents evaporate during annealing, providing no lasting defect passivation[37–39]. Similarly, small organic molecules such as thiophene and pyridine have been used for surface treatments, but weak interaction with the perovskite lattice and volatility limit their long-term effectiveness[33,40]. Consequently, recent efforts have focused on developing robust additives with strong coordination capabilities that can regulate crystal growth, reduce grain boundary defects, and suppress nonradiative recombination by interacting with uncoordinated Pb^{2+} sites[14,41–43].

Herein, we introduce 1H-indole-3-carbohydrazide (1H-CBH) as a multifunctional additive capable of simultaneously modulating the crystallization of perovskites and suppressing defect formation. The molecule features carbonyl and indole moieties strategically distributed across its conjugated structure[44]. Notably, 1H-CBH is a pharmaceutical-grade compound widely used in anticancer therapies, characterized by high chemical stability and strong coordination ability[45]. Distinct from conventional volatile additives, 1H-CBH remains embedded within the perovskite matrix after film formation. Its carbonyl oxygen atoms coordinate with uncoordinated Pb^{2+} ions via lone-pair donation, while the $-NH_2$ groups form hydrogen bonds with the nitrogen atoms of formamidinium (FA^{+}) cations. Moreover, the N–H groups in the indole ring establish N–H···I hydrogen bonds with uncoordinated I^{-} ions. This multimodal passivation mechanism effectively suppresses deep trap states, reinforces grain boundary passivation, and enhances the interfacial compatibility with the electron transport layer. Consequently, the incorporation of 1H-CBH into FA-based perovskite devices significantly improved the PV performance, increasing the PCE from 18.88% to 20.62% and V_{oc} from 1.03 to 1.10 V. For mixed-cation systems (formamidinium/methylammonium, FAMA), the PCE was enhanced from 21.18% to 23.59%, accompanied by elevated V_{oc} (1.15 to 1.18 V) and FF (71.3% to 76.7%). Importantly, large-area (1 cm^2) devices incorporating 1H-CBH achieved a remarkable PCE enhancement from 13.33% to 15.60%, with improved V_{oc} (1.04 to 1.10 V) and FF (60.53% to 67.08%), validating the scalability and practical applicability of incorporating additives into perovskites. The results presented herein demonstrate that 1H-CBH represents a powerful multifunctional additive capable of simultaneously passivating defects, regulating film formation, and enhancing the charge dynamics at the interface, offering a promising pathway toward highly efficient and stable PSCs.

2 Materials and methods

2.1 Materials

Reagents: 1H-indole-3-carbohydrazide (1H-CBH, 97%) was supplied by Shenzhen Yibaishun Technology Co., Ltd. Poly(triarylamine) (PTAA, 99.5%), [6,6]-phenyl-C_{61}-butyric acid methyl ester ($PC_{61}BM$, 99%), bathocuproine (BCP, 99%), cesium iodide (CsI, 99.5%), lead(II) iodide (PbI_2, 99.8%), and formamidine iodide (FAI, 99%) were purchased from Xi'an Yuri Solar Co., Ltd. Methylammonium iodide (MAI, 99%) was sourced from Greatcell Solar; and silver (Ag, 99.99%) was acquired from Zhongnuo New Materials (Beijing) Technology Co., Ltd.

Solvents: Dimethylformamide (DMF, 99.8%), dmethyl sulfoxide (DMSO, 99.9%), tin(IV) oxide (SnO_2, 99.9%), and chlorobenzene (CB, 99.9%) were supplied by Sigma-Aldrich. Isopropanol (IPA, 99.8%) was purchased from Macklin. Ethanol (C_2H_5OH, 99%) and acetone (C_3H_6O, 98%) were purchased from Shenzhen Chemical Technology Co., Ltd. Toluene (TL, 99%) was obtained from Guangzhou Brand Co., Ltd.

2.2 Preparation of precursor

The precursor solution for $Cs_{0.15}FA_{0.85}PbI_3$ was prepared by dissolving PbI_2, CsI, and FAI in 1 mL of a mixture comprising DMF and DMSO (4:1, volume/volume). The reaction mixture was stirred overnight at 60°C and filtered after cooling to room temperature. 1H-CBH was added to the precursor solution at respective concentrations of 0.5, 1.0, 1.5, and 2.0 mg mL^{-1}. As evidenced by the full-width-at-half-maximum (FWHM) of the (110) diffraction peak (Fig. S5 in the Electronic Supplementary Material [ESM]), incorporation of the additive at a concentration of 1.0 mg mL^{-1} yielded the narrowest FWHM and largest crystallite size, whereas higher concentrations (≥1.5 mg mL^{-1}) induced significant FWHM broadening, indicating reduced crystallinity. Consequently, 1.0 mg mL^{-1} was selected as the optimal concentration for subsequent incorporation into all films and devices (labeled 1H-CBH); controls were prepared without the additive.

Similarly, the precursor solution for $Cs_{0.15}(FA_{0.8}MA_{0.2})_{0.85}PbI_3$ was prepared by dissolving MAI, PbI_2, CsI, and FAI in 1 mL of a DMF and DMSO mixture (4:1, volume/volume), followed by stirring overnight at 60°C and filtration after cooling to room temperature. The precursor solution was prepared by incorporating 1H-CBH at 1.0 mg mL^{-1} (designated as the target sample, 1H-

CBH); the identical solution without 1H-CBH served as the control.

2.3 Device fabrication

The architecture of the inverted (p-i-n) perovskite solar cell studied herein comprises ITO/PTAA/Perovskite/$PC_{61}BM$/BCP/Ag. The ITO glass substrate was completely cleaned with ethanol, deionized water, and acetone under sonication for 20 min each. After drying in an electric thermostatic drying oven, the substrate was treated with oxygen-plasma for 120 s to confer hydrophilicity to the surface. PTAA solution (2 mg mL^{-1}, dissolved in toluene) was spin-coated onto ITO substrate at 5,000 rpm for 20 s, followed by annealing at 110°C for 10 min in a glove-box under nitrogen atmosphere. After cooling to room temperature, the perovskite precursor solution was spin-coated onto the PTAA substrate at a speed of 1,000 rpm for 8 s and 5,000 rpm for 30 s. After 20 s of spin-coating at 5,000 rpm, 100 μL of CB was deposited onto the substrate and then annealed at 100°C for 30 min. After cooling, $PC_{61}BM$ solution (20 mg mL^{-1}) was deposited onto the perovskite film via spin-coating at 2,000 rpm for 30 s. Afterward, 0.5 mg BCP in 1 mL IPA solution was deposited on the $PC_{61}BM$ film at 2,000 rpm for 30 s. Finally, the device was transferred into a vacuum chamber for deposition of the Ag (100 nm) electrode under a base pressure of 4.0×10^{-4} Pa.

2.4 Characterizations of films

Scanning electron microscope (SEM) observations were performed using a Hitachi S4800 (Hitachi, Japan) instrument. X-ray diffraction (XRD) analyses were conducted at room temperature in reflection mode (D8 FOCUS, Cu Kα radiation, λ = 0.154056 nm). Ultraviolet-visible absorption (UV-Vis) spectra of the thin films were acquired using a HP 8453 spectrophotometer. As light passes through a substance, its degree of absorption varies with the wavelength of the light. By measuring the absorbance of the substance at different wavelengths and plotting the relationship between the absorbance and wavelength, the absorption spectrum of the substance can be obtained. Photoluminescence (PL) spectra of the thin film were collected using a HORIBA Jobin Yvon Lab RAM HR800 instrument with a 532 mm laser source. Ultraviolet photoelectron spectroscopy (UPS) data for the thin films were recorded using a ThermoFisher Escalab Xi+ instrument. Atomic force microscopy (AFM) data were acquired using a Bruker Mutimode8 (Bruker, Germany) instrument. Density functional theory (DFT) calculations were performed using Gaussian 6 software at the B3LYP/6-31G(d,p) level. Visualization of the molecular orbitals and surface electrostatic potential (ESP) distribution was performed using GaussView 9. Time-resolved photoluminescence (TRPL) spectra were collected using a 365 nm Nanosecond pulsed diode laser (Edinburgh instruments, Spectrofluorometer FS5). Contact angle measurements were performed using a DSA30 (Kruss) instrument. Fourier-transform infrared (FTIR) spectra were acquired using a Nicolet iS50 (Thermo Scientific) instrument. X-ray photoelectron spectroscopy (XPS) analyses of the perovskite films were performed using Thermo Fisher ESCALAB 250 Practice equipment. Grazing-incidence wide-angle X-ray scattering (GIWAXS) measurements were implemented using SAXS Focus 3.0. This measurement system features a Cu X-ray source (8.05 keV, 1.54 Å) coupled with an EIGER 2R 500K detector for signal collection.

2.5 Characterization of the devices

Current density–voltage (*J*–*V*) curves of the PSCs were obtained using a 2400 Series Source Meter (Keithley Instruments) measurement unit (Newport, Oriel AM 1.5 G, 100 mW cm^{-2}); the accuracy was calibrated using an NREL standard Si cell. The measurements were performed by voltage scanning from −0.2 to 1.2 V (forward). The external quantum efficiency (EQE) was quantified using a QE Measurement System (SCS1011-QZU) from Zolix Instrument Co., Ltd. Electrochemical impedance spectroscopy (EIS) analyses were performed using an electrochemical workstation (SP-300, Bio-Logic). The current–voltage (*I*–*V*) characteristics of the PSCs were determined under dark conditions using an *I*–*V* testing system (YSL SCpro7, Zolix). The system consisted of optical and electrical parts. The space-charge-limited current (SCLC) method was adopted to confirm the decrease in the trap density within the perovskite film. For the experiment, electron-only devices were constructed, and their configuration was designed as ITO/SnO_2/Perovskite/$PC_{61}BM$/BCP/Ag. The defect density in the semiconductor was determined by analyzing the *I*–*V* curve in the region corresponding to space-charge-injected current. The capacitance–voltage (*C*–*V*) curves can be directly compared to the built-in potential (V_{bi}) of the devices determined using the Mott–Schottky equation. Stability testing was conducted under ambient conditions (25°C, 25% RH). The device performance was continuously monitored at the maximum power point under simulated AM 1.5G solar irradiation equivalent to one-sun intensity.

3 Results and discussion

DFT calculations were performed at the B3LYP/6-31G(d,p) level to investigate the frontier orbital distribution and ESP of the 1H-CBH molecule (Fig. S1a in the ESM). As shown in Fig. S1b in the ESM, the carbonyl oxygen atom and amino nitrogen exhibit strong electronegativity, whereas the indole moiety presents relatively positive electrostatic potentials. This distinct charge distribution suggests that the carbonyl oxygen in 1H-CBH readily donates electron density to uncoordinated Pb^{2+}, forming C=O···Pb coordination interactions. Simultaneously, the N–H group within the indole unit can form N–H···I hydrogen bonds with uncoordinated I^- in the perovskite lattice. Moreover, the amino nitrogen ($-NH_2$) can donate electron density to the hydrogen atoms of the FA^+ cations, forming H–N···H hydrogen bonds. The calculated highest occupied molecular orbital and lowest unoccupied molecular orbital energy levels of 1H-CBH are −6.06 eV and −0.57 eV, respectively (Fig. S2 in the ESM). Collectively, these multi-site interactions anchor 1H-CBH at the grain boundaries and surface regions, enhancing defect passivation and improving the interfacial contact between the perovskite absorber and electron-transport layer. The detailed interaction mechanisms are illustrated

in Figs. S3 and S4 in the ESM.

The influence of 1H-CBH on the morphology of the perovskite film was evaluated via SEM and AFM analyses. The top-view SEM images (Figs. 1a and 1b) reveal that the pristine $Cs_{0.15}FA_{0.85}PbI_3$ films display pronounced grain boundaries and numerous pinholes, whereas the 1H-CBH-modified films exhibit significantly enlarged grain sizes (Fig. 1c). Table S1 in the ESM presents the particle-size distribution derived from top-view SEM images of the perovskite thin films. Upon incorporation of the 1H-CBH additive, the average grain size increased from 221.3 to 235.3 nm, with a notable improvement in the minimum grain size (from 139.8 to 170.2 nm). The narrowing of the grain-size distribution directly reflects a more homogeneous perovskite microstructure, yielding a denser film with a lower density of morphological defects and enhanced structural continuity. AFM imaging further confirmed this improvement, with the root-mean-square roughness decreasing from 16.9 nm for the pristine film to 10.9 nm upon incorporation of 1.0 mg mL^{-1} 1H-CBH (Figs. 1d and 1e). The smoother film surface enhances physical contact with the electron-transport layer, thereby facilitating more efficient charge separation and electron transport. The crystallinity of the modified films was evaluated using XRD (Fig. 1f). No notable peak shifts were observed, indicating that 1H-CBH is not incorporated into the perovskite lattice. This behavior is attributed to the relatively large molecular size of 1H-CBH, which prevents lattice integration and allows localization of the molecule at the grain boundaries via interactions with uncoordinated Pb^{2+} and uncoordinated I^-[46]. To further quantify crystallite size evolution, the FWHM of the (110) diffraction peak was analyzed using the Scherrer equation (Eq. 1).

$$D = \frac{K\lambda}{\beta \cos\theta} \tag{1}$$

Here, D denotes the average crystallite size, K is the shape factor (typically 0.9), λ is the X-ray wavelength (1.5406 Å for Cu-Kα radiation), β is the FWHM after correction for instrumental broadening, and θ is the Bragg diffraction angle. According to the Scherrer equation, smaller crystallite sizes inherently produce broader diffraction peaks (i.e., larger FWHM values), reflecting the inverse relationship between the crystallite size and peak broadening. As shown in Fig. S5 in the ESM, the perovskite film treated with 1.0 mg mL^{-1} 1H-CBH exhibited the narrowest FWHM for the (110) reflection, corresponding to the largest calculated crystallite size. This observation indicates that optimal crystallinity and grain growth are achieved at this additive concentration. However, further increasing the additive concentration to 1.5 mg mL^{-1} resulted in a noticeable increase in the FWHM, suggesting a reduction in the crystallite size and partial deterioration of the crystal quality. This trend suggests that excessive additive loading disrupts the crystallization process, plausibly owing to competitive coordi-

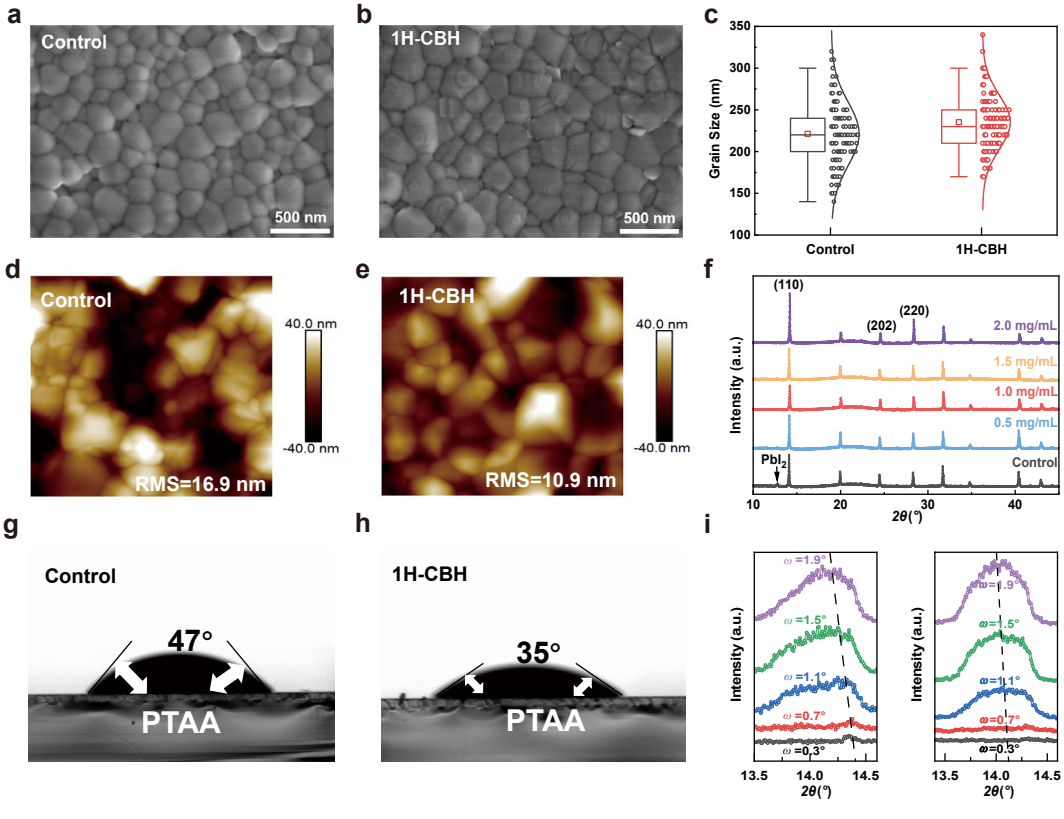

Figure 1 Improved perovskite crystallization with 1H-CBH. (a–b) Top-view SEM images of control (a) and 1H-CBH-treated (b) perovskite films. (c) Grain-size distribution of perovskite films with and without 1H-CBH. (d–e) AFM height maps of control (d) and 1H-CBH-treated (e) films. (f) XRD patterns of perovskite films with varying 1H-CBH concentrations. (g–h) Contact angles of control (g) and 1H-CBH-modified (h) perovskite films with HTL (PTAA). (i) GIXRD patterns at different incident angles for control (left) and 1H-CBH-treated (right) samples.

nation or accumulation of residual stress within the perovskite lattice. Based on these results, 1.0 mg mL^{-1} was identified as the optimal 1H-CBH loading level; therefore, all target films and devices in this study were fabricated using this concentration and are denoted simply as 1H-CBH. Control samples were prepared without the additive. GIWAXS was used to further elucidate the structural evolution induced by 1H-CBH. As shown in Figs. S6a and S6b in the ESM, the control sample displayed dominant diffraction features at q = 0.01 nm^{-1} and q = 1.39 nm^{-1}, corresponding to the (110) and (220) perovskite phases, respectively. Remarkably, the incorporation of 1H-CBH significantly enhanced the intensity of all characteristic peaks, providing direct evidence of improved crystallinity and higher phase-purity. This enhancement suggests a more complete transformation of nonideal phases into the thermodynamically favored α-phase perovskite, a structural configuration well correlated with superior photovoltaic performance[46,47]. The interfacial wettability and surface characteristics were evaluated through contact angle measurements, revealing a pronounced decrease in the contact angle on the PTAA hole-transport layer upon the addition of 1H-CBH (Figs. 1g and 1h). This change indicates improved wettability of the HTL surface by the perovskite precursor. This enhanced interfacial compatibility is particularly beneficial for achieving uniform film deposition over large areas[17]. The residual strain characteristics were further probed using GIXRD at varying angles (ω), as shown in Fig. 1i. The control films exhibited obvious peak shifts toward lower diffraction angles with increasing ω, indicating substantial tensile stress within the lattice[48]. In contrast, the lattice spacing of the 1H-CBH-modified films showed negligible variation across the probing depths, confirming effective dissipation of the residual strain through structural reconfiguration. This strain-relief mechanism mitigates lattice distortion, suppresses defect formation, and contributes to the enhanced PCE and improved operational stability of the resulting PSCs.

FTIR spectroscopy was employed to clarify the interfacial interactions between 1H-CBH and the perovskite lattice. As shown in Fig. 2a, both the pristine and 1H-CBH-modified perovskite films exhibit characteristic vibrational features consistent with previous reports[49]. A distinct blue-shift of the C=O stretching vibration from 1,613 to 1,621 cm^{-1} was observed after introducing 1H-CBH into the perovskite system. This shift signifies strong chemical coupling between the carbonyl groups of 1H-CBH and PbI_2 species, in line with the proposed defect-passivation mechanism. Additional insight into the coordination behavior of Pb^{2+} was obtained through XPS. The Pb 4f spectra (Fig. 2b) show Pb $4f_{5/2}$ and Pb $4f_{7/2}$ peaks at 143.12 and 138.24 eV, respectively, for which noticeable binding-energy shifts were observed with the incorporation of 1H-CBH, indicating a modified electronic environment surrounding the lead ions. The O 1s spectra (Fig. 2c) further support this observation, with the C=O-related signal moving from 532.15 eV in the spectrum of the pristine film to 532.78 eV in that of the 1H-CBH-treated sample. This 0.63 eV upshift provides direct evidence of coordination between the carbonyl oxygen atoms and uncoordinated Pb^{2+} ions. Changes in the I 3d spectra (Fig. 2d) reveal additional interactions. The I $3d_{3/2}$ and I $3d_{5/2}$ peaks at 630.54 and 619.09 eV shifted upon the introduction of 1H-CBH, reflecting modifications in the local electronic environment of uncoordinated I^- within the perovskite lattice. The complementary changes in the N 1s region (Fig. 2e), with the N–H signal occurring at 400.56 eV for the 1H-CBH/perovskite system compared to 400.41 eV for the pristine sample, confirm the formation of H–N···H hydrogen bonds between the $-NH_2$ moieties and the hydrogen atoms of FA^+. The C 1s spectra of the

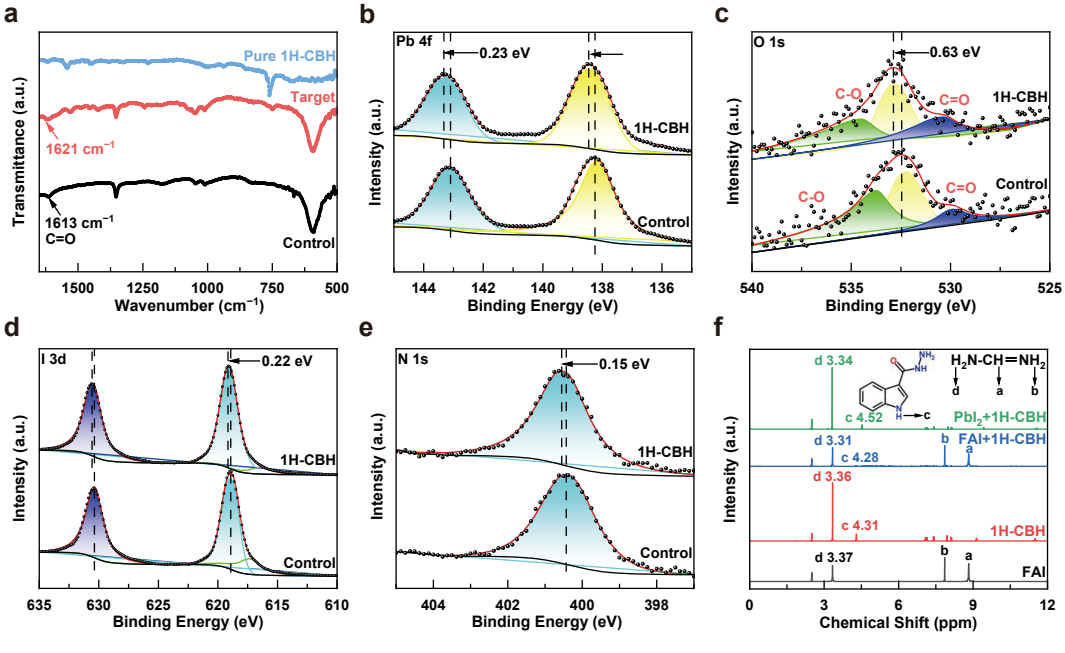

Figure 2 Molecular interactions between 1H-CBH and perovskite. (a) FTIR spectra of pure 1H-CBH, 1H-CBH + perovskite, and perovskite. (b–e) Pb 4f (b), O 1s (c), I 3d (d), and N 1s (e) XPS profiles of unpassivated and 1H-CBH-passivated perovskite films. (f) ^1H NMR spectra of pure FAI, pure 1H-CBH, 1H-CBH + PbI_2, and 1H-CBH + FAI.

control and treated samples (Fig. S7 in the ESM) remained unchanged, confirming that the carbon centers do not participate in coordination. These spectroscopic results collectively indicate that the interfacial interactions mainly involve the coordination of carbonyl oxygen atoms with Pb^{2+} and hydrogen bonding between the indole moiety and I^- ions. ^1H nuclear magnetic resonance (NMR) spectroscopy was further used to examine the interactions among FAI, 1H-CBH, and PbI_2 in DMSO-d_6 solution. As illustrated in Fig. 2f, the proton signals of the –CH (a) and $-NH_2$ (b) groups in FAI remained unaffected by the incorporation of 1H-CBH. In contrast, the signal of the $-NH_2$ protons (d) of FAI shifted upfield by 0.06 ppm (δ changed from 3.37 to 3.31 ppm), providing clear evidence of hydrogen bonding between the amino nitrogen of 1H-CBH and the FA^+ cations. The N–H signal (c) of the indole unit in 1H-CBH also underwent substantial changes, exhibiting a prominent downfield shift of 0.21 ppm (δ changed from 4.31 to 4.52 ppm) after PbI_2 addition, whereas a slight upfield shift of 0.03 ppm (δ changed from 4.31 to 4.28 ppm) was observed with FAI. These observed changes verify direct chemical interactions between the indazole ring of 1H-CBH and PbI_2, as well as hydrogen bonding with the amino group and FA^+, in excellent agreement with the previous XPS findings[50].

To assess the influence of 1H-CBH on the device performance, inverted-structure PSCs (Fig. 3a) were fabricated using $Cs_{0.15}FA_{0.85}PbI_3$ as the absorber layer; 1H-CBH was incorporated at a concentration of 1.0 mg mL^{-1}. The resulting *J*–*V* curves are displayed in Fig. 3b. The devices treated with 1H-CBH showed a pronounced performance enhancement, with an increase in the V_{oc} from 1.03 to 1.10 V and the PCE from 18.88% to 20.62%. These enhancements originate from the substantial reduction of nonradiative recombination losses. In the control devices, the high defect density provides recombination centers, thereby accelerating trap-mediated carrier loss, limiting the achievable V_{oc}. When 1H-CBH is incorporated, its carbonyl oxygen atoms form strong coordination bonds with uncoordinated Pb^{2+} ions, whereas the hydrogen atoms of the indazole ring engage in hydrogen bonding with uncoordinated I^- ions. These dual interactions suppress defect formation, minimize trap-assisted recombination, and promote more efficient charge extraction. Consequently, nonradiative energy losses are significantly reduced, leading to a larger QFLS and ultimately higher V_{oc} and PCE. The integrated J_{sc} derived from the EQE spectrum corresponds precisely to the J_{sc} value obtained

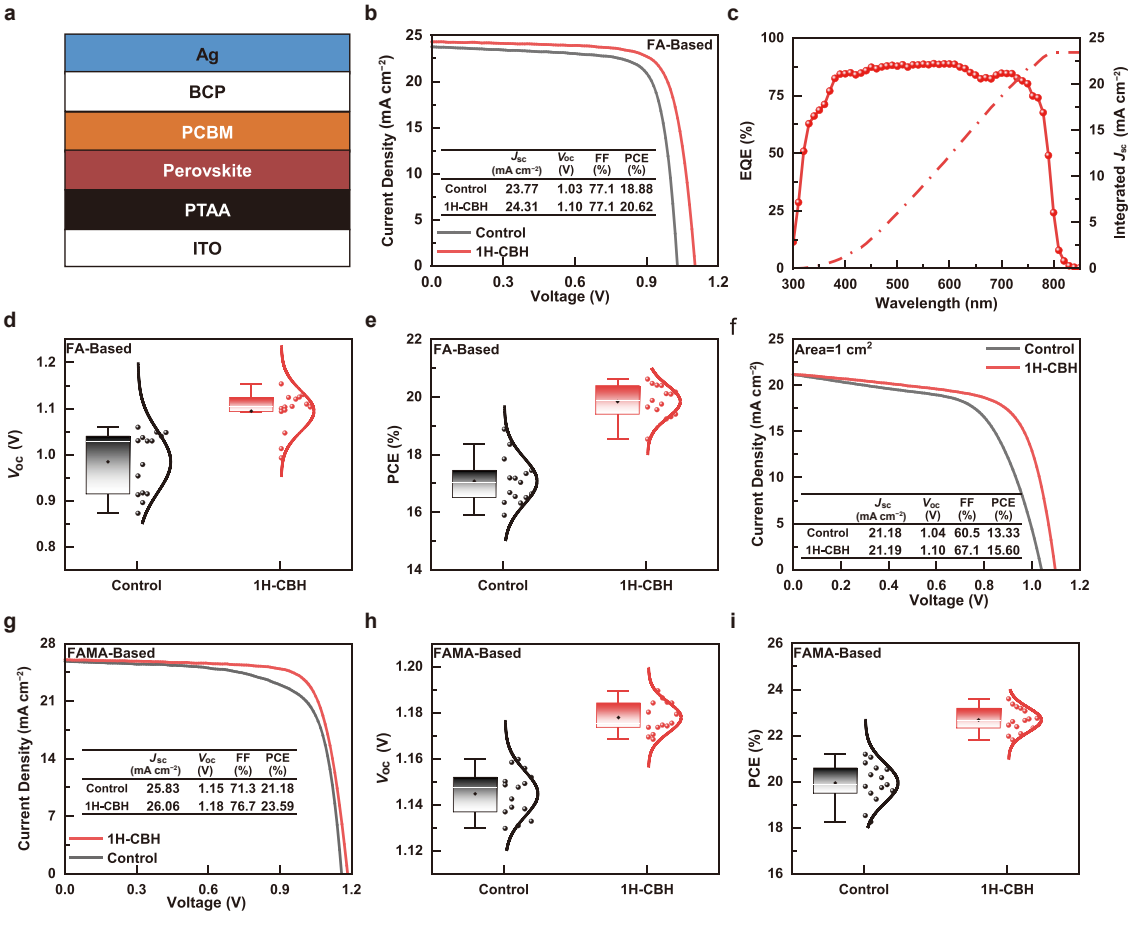

Figure 3 Photovoltaic performance of perovskite solar cells. (a) Schematic of the device structure. (b) *J*–*V* characteristics of FA-based perovskite solar cells without and with 1H-CBH. (c) EQE spectrum and integrated J_{sc} values for 1H-CBH-treated device. (d–e) V_{oc} (d) and PCE (e) distributions of FA-based PSC without and with 1H-CBH additive. (f) *J*–*V* characteristics of 1 × 1 cm^2 perovskite solar cells without and with 1H-CBH. (g) *J*–*V* characteristics of FAMA-based PSCs without and with 1H-CBH. (h–i) V_{oc} (h) and PCE (i) distributions of FAMA-based PSC without and with 1H-CBH additive.

from *J*–*V* characterization of the device employing 1H-CBH (Fig. 3c). The statistics for the parameters from 15 devices (Figs. 3d and 3e, Figs. S8a and S8b in the ESM) further demonstrate the consistent enhancement achieved through 1H-CBH incorporation, particularly in the V_{oc}.

Contact angle measurements reveal that 1H-CBH markedly improves the wettability of the PTAA surface toward the perovskite precursor solution. Better interfacial compatibility facilitates the deposition of uniform films, which is especially important for the fabrication of large-area devices. Motivated by this advantage, PSCs with an active area of 1 cm^2 were fabricated. The *J*–*V* curves in Fig. 3f show that 1H-CBH again provides clear benefits. The V_{oc}, FF, and PCE increased from 1.04 to 1.10 V, 60.53% to 67.08%, and 13.33% to 15.60%, respectively. These results underscore the strong potential of 1H-CBH as a robust additive for achieving high-performance, large-area PSCs and highlight its relevance for scalable manufacturing. Incorporating 1H-CBH markedly enhanced the FF of large-area PSCs, an improvement attributed to the FF's heightened sensitivity to interfacial defects. The FF is critically governed by the charge-transport efficiency and recombination dynamics within the device. Notably, the 1H-CBH additive effectively mitigates deep trap states, thereby enhancing the charge-carrier mobility, as substantiated by subsequent SCLC measurements. Concurrently, the introduction of 1H-CBH suppresses trap-assisted nonradiative recombination in the perovskite layer, a finding strongly corroborated by the PL and TRPL analyses. These systematic investigations collectively establish 1H-CBH as a promising candidate for optimizing charge-transport pathways and minimizing recombination losses in high-performance PSCs. Furthermore, the compatibility of this additive with scalable, large-area device fabrication processes underscores its significant potential for industrial-level applications in next-generation photovoltaic technologies.

The general applicability of 1H-CBH was further examined using mixed-cation FAMA perovskite devices ($Cs_{0.15}(FA_{0.8}MA_{0.2})_{0.85}PbI_3$), in which MA^+ was introduced alongside FA^+ and Cs^+. The control devices delivered a champion PCE, V_{oc}, J_{sc}, and FF of 21.18%, 1.15 V, 25.83 mA cm^{-2}, and 71.3%, respectively (Fig. 3g). After incorporating 1H-CBH, the champion PCE increased to 23.59%, accompanied by an improvement in the V_{oc} to 1.18 V and a rise in the FF to 76.7%. The statistical data from 15 devices (Figs. 3h and 3i, Figs. S9a and S9b in the ESM) confirm that the performance enhancement is highly reproducible. The simultaneous improvements in the V_{oc} and FF align well with the mechanistic understanding established earlier. Additive-induced suppression of ion migration, reduction of the trap density, and the passivation of uncoordinated Pb^{2+} and I^- defects contribute to mitigating nonradiative recombination, thereby enabling higher photovoltaic efficiency.

The SCLC technique was utilized to systematically quantify variations in the trap density of the perovskite films with and without 1H-CBH modification, demonstrating a direct correlation between defect passivation and enhancements in the device performance[51]. The trap-filled limit voltage (V_{TFL}) was determined from the intersection of the Ohmic and trap-filled limit regions in the *I*–*V* curves. Electron-dominated devices with the ITO/SnO_2/Perovskite/PCBM/BCP/Ag (Fig. 4a) architecture were fabricated and their *I*–*V* characteristics were measured at applied voltages in the range of 0–1 V. As shown in Fig. 4b, the V_{TFL} of the pristine perovskite device was 0.21 V but decreased dramatically to 0.11 V for the 1H-CBH-passivated device. This reduction indicates a substantial decrease in the defect density within the perovskite layer. $N_{defects}$ and $\mu_{electron}$ were calculated using Eqs. 2 and 3, respectively.

$$N_{defects} = \frac{2\varepsilon\varepsilon_0 V_{TFL}}{eL^2} \tag{2}$$

$$\mu_{electron} = \frac{8L^3K}{9\varepsilon\varepsilon_0} \tag{3}$$

Here, ε_0 and ε denote the vacuum permittivity and dielectric constant of the perovskite, respectively; e and L represent the electron charge and thickness of the perovskite film, respectively; and K denotes the slope of the Child regime. For $Cs_{0.15}FA_{0.85}PbI_3$, ε = 23[52] and L = 110 nm[53]. The trap density of the pristine perovskite film (4.42×10^{16} cm^{-3}) was significantly reduced to 2.31×10^{16} cm^{-3} upon 1H-CBH incorporation, as summarized in Table S2 in the ESM. Concurrently, the electron mobility increased from 3.89×10^{-4} to 6.16×10^{-4} cm^2 V^{-1} s^{-1}, confirming enhanced charge transport. These results align with the observed suppression of nonradiative recombination, leading to improved photovoltaic performance.

UPS was used to confirm the improved band alignment in PSCs, induced by incorporation of the 1H-CBH additive. The results are presented in Figs. S10a and S10b in the ESM. The valence band maximum shifted from −5.99 eV for the pristine film to −5.89 eV after 1H-CBH treatment. Combined with the bandgap (~1.53 eV, Fig. S11 in the ESM) derived from the UV-Vis absorption spectra (Fig. 4c), the conduction band minimum energies were calculated as −4.46 and −4.36 eV for the control and 1H-CBH-modified films, respectively. Notably, although the absorption onset remained unaltered, the light-absorption intensity was significantly enhanced, demonstrating that 1H-CBH does not modify the intrinsic bandgap but improves the light-harvesting efficiency, thereby promoting higher photocurrent generation. The corresponding energy level diagram is illustrated in Fig. S12 in the ESM, revealing that the 1H-CBH-treated perovskite film exhibits more n-type-like electronic character. This favorable band alignment facilitates efficient electron extraction at the interface, aligning closely with the earlier discussion on the enhanced device performance. PL spectroscopy analysis of the perovskite films deposited on glass substrates (Fig. 4d) showed a pronounced increase in the PL intensity for the 1H-CBH-modified film, indicating effective suppression of defect-mediated nonradiative recombination through 1H-CBH passivation[54]. The PL spectra of the 1H-CBH-modified films display a minimal red-shift of 2 nm relative to that of the control, consistent with the negligible spectral shifts observed in the UV-Vis absorption. This minor shift is insignificant in the context of device performance metrics. Additionally, the excitonic behavior of the 1H-CBH-modified perovskite films was evaluated using TRPL spectroscopy (Fig. 4e). The TRPL decay curves were fitted

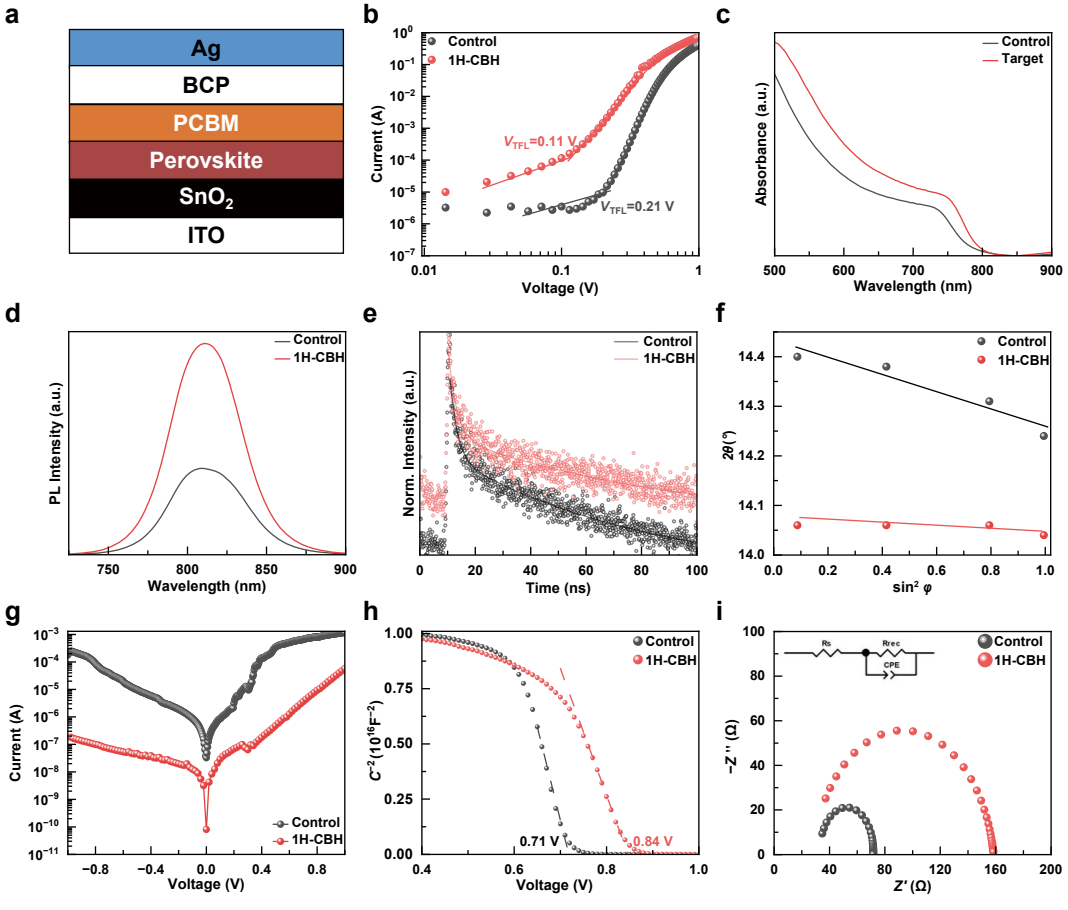

Figure 4 Role of 1H-CBH in structure–property relationships. (a) Schematic of electron-only device structure. (b) SCLC curves of perovskite solar cells without and with 1H-CBH. (c) UV-Vis absorption spectra of perovskite films without and with 1H-CBH. (d) PL spectra of perovskite films without and with 1H-CBH. (e) TRPL spectra of perovskite films without and with 1H-CBH. (f) d-Spacing as a function of grazing incidence angle for control and 1H-CBH-modified perovskite films. (g) Dark *I*–*V* curves for PSCs without and with 1H-CBH. (h) M-S curves for PSCs without and with 1H-CBH. (i) EIS profiles of PSCs without and with 1H-CBH.

to a biexponential decay function. The extracted parameters are summarized in Table S3 in the ESM. The fast decay time (τ_1), which represents trap-assisted nonradiative charge recombination, and the slow decay time (τ_2), which is associated with radiative charge recombination, were obtained[55]. For the pristine $Cs_{0.15}FA_{0.85}PbI_3$ perovskite, τ_1 = 2.70 μs and τ_2 = 75.75 μs, whereas the lifetimes were longer for the 1H-CBH-modified perovskite, where τ_1 = 2.87 μs and τ_2 = 80.43 μs. The average carrier lifetime (τ_{ave}) was calculated using Eq. 4.

$$\tau_{ave} = \frac{\sum A_i \tau_i^2}{\sum A_i \tau_i} \quad (4)$$

The increase in τ_{ave} from 74.07 μs to 77.81 μs confirms effective suppression of nonradiative recombination. This enhancement directly contributes to the increase in the V_{oc} and overall device efficiency. The residual strain in the perovskite films was quantified by linear regression of 2θ as a function of $\sin^2\varphi$, where the slope of the fitted line directly reflects the magnitude of the residual strain (Fig. 4f). A positive slope indicates compressive stress, whereas a negative slope corresponds to tensile strain. For the pristine perovskite films, the linear fit yielded a distinct negative slope, confirming the presence of intrinsic tensile strain. In contrast, the slope was markedly reduced for the 1H-CBH-modified films, demonstrating substantial strain relaxation in the films[56]. This observation aligns closely with the GIXRD patterns of the control and 1H-CBH-treated films recorded at varying incident angles, collectively validating that 1H-CBH incorporation effectively mitigates lattice strain in the films and enhances the structural stability.

A deeper understanding of the influence of 1H-CBH on the charge-transport behavior was obtained through systematic analysis of the dark *I*–*V* characteristics of the PSCs. This measurement provides direct insight into the carrier recombination and defect-assisted transport processes under nonilluminated conditions. By comparing the dark-current responses of the control and 1H-CBH-modified devices, changes in the diode quality, leakage current, and trap-assisted recombination pathways can be clearly resolved, enabling more comprehensive assessment of how the additive regulates the charge dynamics within the device structure (Fig. 4g). Notably, the dark-current density was significantly reduced from 5.45 × 10^{-7} mA cm^{-2} in the control device to 1.35 × 10^{-9} mA cm^{-2} after modification with 1H-CBH, indicating effective suppression of the leakage currents and enhanced interfacial charge transport. This observation strongly suggests

that the passivation of interfacial defects induced by 1H-CBH plays a critical role in improving the charge-extraction efficiency[57]. M–S analysis was also performed to determine the built-in potential (V_{bi}) of the PSCs (Fig. 4h). The built-in potential was estimated using Eq. 5.

$$\frac{A^2}{C^2} = \frac{2(V_{bi} - V)}{q\varepsilon\varepsilon_0 N} \quad (5)$$

Here, A, C, V, q, ε, ε_0, and N represent the active area, capacitance, applied voltage, electric charge, perovskite dielectric constant, vacuum permittivity, and charge-carrier density, respectively. The extracted V_{bi} values for pristine $Cs_{0.15}FA_{0.85}PbI_3$ and the 1H-CBH-modified perovskite are 0.71 and 0.84 V, respectively. This notable increase in the built-in potential confirms strengthening of the internal electric field, which facilitates more efficient charge separation and collection, contributing to the observed enhancement in the V_{oc}. EIS was used to investigate the charge-transfer kinetics in the PSCs (Fig. 4i, and Table S4 in the ESM). The experimental and fitting results revealed that after 1H-CBH modification, the series resistance (R_s) decreased from 33.42 to 27.57 Ω, which directly contributed to the improved J_{sc}[58,59], while the recombination resistance (R_{rec}) increased from 38.05 Ω to 131.00 Ω. This significant enhancement in R_{rec} indicates that nonradiative recombination is effectively suppressed upon introducing the 1H-CBH additive. These observations align consistently with the earlier analysis of the defect passivation and reduced nonradiative recombination mechanisms.

Systematic evaluation of the impact of 1H-CBH on the device stability was conducted under humid air environment (25°C, 50%–80% relative humidity) and dry N_2 atmosphere without encapsulation of the devices. XRD analyses after 8 months of ambient storage revealed a dramatic increase in PbI_2 phase within unpassivated perovskite films, whereas PbI_2 formation was significantly suppressed in the 1H-CBH-passivated films (Figs. 5a and 5b). This observation indicates that surface passivation by 1H-CBH effectively mitigates decomposition of the crystalline structure in perovskites. Furthermore, the XRD patterns of the 1H-CBH-treated films retained the characteristic diffraction peaks of the stable hexagonal phase, whereas the pristine films underwent a phase transition to the unstable β-phase[60]. Visual inspection of the perovskite films after 8 months under ambient conditions revealed severe degradation of the unpassivated samples, with complete transparency (Fig. S13 in the ESM), whereas the initial morphology and structural integrity were maintained in the passivated films, consistent with the XRD data. In the stability test under controlled N_2 atmosphere, PSCs incorporating 1H-CBH retained over 80% of their initial PCE after 600 h of continuous storage. In contrast, the pristine devices exhibited 20% PCE degradation within 150 h under identical conditions (Fig. 5c). These results

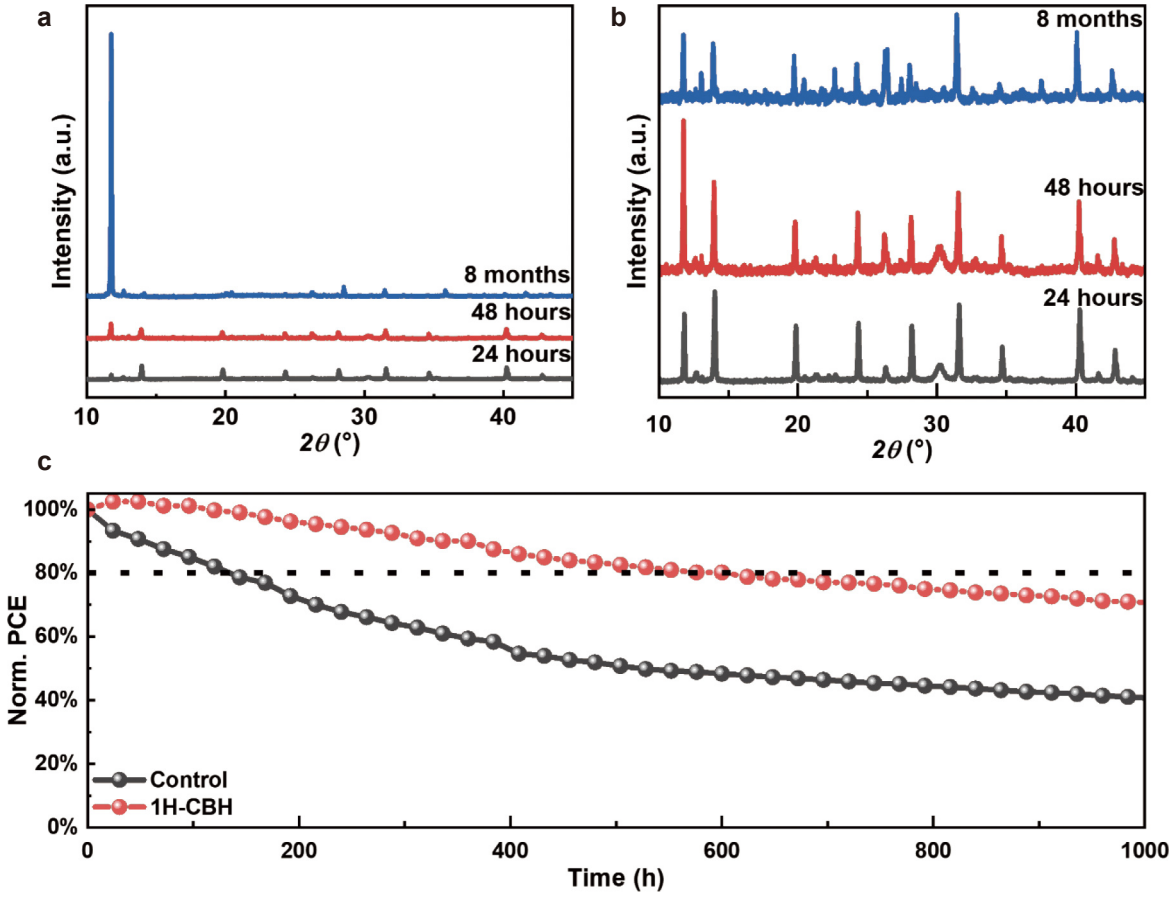

Figure 5 Stability test. (a–b) XRD patterns of the perovskite films without (a) and with (b) 1H-CBH additive after 24 h, 48 h and 8 months of aging at 25°C and 50%–80% relative humidity under ambient atmosphere. (c) Stability of the corresponding perovskite solar cells without encapsulation in a N_2-filled environment with 25% relative humidity at 25°C.

demonstrate that 1H-CBH passivation not only enhances the intrinsic stability of the material through defect passivation but also improves the resistance to the environment, thereby significantly prolonging the operational lifespan of the device.

To further investigate the impact of continuous illumination on the device stability, the perovskite films were systematically characterized at 10 min intervals under a light intensity of 1,000 mW cm^{-2} (10 suns) (Figs. S14a–S14d in the ESM). The film incorporating 1H-CBH additive demonstrated superior stability after 1 h of illumination, in stark contrast to the control sample, which exhibited significant degradation. Notably, the (110) diffraction peak of the control film shifted markedly toward lower diffraction angles, whereas that of the 1H-CBH-modified film displayed a substantially smaller shift. The observed leftward shift of the diffraction peaks under illumination is attributed to halide migration, wherein the perovskite phase separates into iodide-rich (I-rich) and iodide-vacancy domains upon exposure to light[61]. Given the large ionic radius of iodide, the formation of I-rich regions likely induces lattice expansion, resulting in a shift of the diffraction peak to lower angles. Such lattice expansion is closely linked to severe degradation in the device stability. However, the lattice expansion observed in the 1H-CBH-passivated film was significantly suppressed, providing direct evidence that the –NH group of the indole moiety in 1H-CBH forms hydrogen-bonding interactions with I^- in the perovskite lattice. This interaction effectively mitigates halide migration under illumination, preventing the formation of I-rich domains and enhancing the overall device stability. Previous studies have reported simultaneous broadening of the Bragg peaks and the emergence of additional low-angle peaks in the XRD patterns during halide segregation, confirming the generation of I-rich perovskite domains[62]. In our experiments, broadening of the Bragg peak was observed for both the control and 1H-CBH-modified films. However, the extent of broadening was markedly reduced in the case of the 1H-CBH-treated sample, further supporting the conclusion that 1H-CBH suppresses light-induced halide segregation and the associated formation of I-rich regions. These findings highlight the broader significance of additive engineering in mitigating halide-segregation-induced lattice distortions, where synergistic passivation through coordination bonds and hydrogen-bond interactions plays a pivotal role in stabilizing perovskites under operational conditions. By strategically designing additives capable of forming both coordination and hydrogen bonds, this multi-passivation strategy effectively suppresses ion migration, phase separation, and crystallinity degradation.

4 Conclusion

This study demonstrates the use of 1H-indole-3-carbohydrazide as a multifunctional additive for defect passivation and performance optimization in PSCs. Through comprehensive morphological, spectroscopic, and electrical characterization, we unveil a multi-passivation mechanism in perovskite systems. First, coordination bonding between the carbonyl oxygen atoms and uncoordinated Pb^{2+} ions effectively passivates metal-related defects. Second, hydrogen bonding interactions between the –NH group of the indole moiety and uncoordinated I^- suppress halide-related trap states. Finally, the $-NH_2$ groups form H–N···H hydrogen bonds with hydrogen atoms in the FA cation of the perovskite lattice, further stabilizing the crystal structure. This synergistic passivation strategy systematically eliminates deep trap states, minimizes nonradiative recombination losses, and enhances the interfacial compatibility with the electron-transport layer. Consequently, this multifunctional additive engineering approach significantly improves the charge extraction efficiency and optimizes the energy level alignment, establishing a robust framework for high-performance perovskite optoelectronics. The incorporation of 1H-CBH (1.0 mg mL^{-1}) into FA-based perovskite devices results in a significant increase in the PCE from 18.88% to 20.62%, attributable mainly to the enhancement of the V_{oc} from 1.03 to 1.10 V. The multi-passivation mechanism demonstrates broad applicability, as evidenced by the enhancement of the PCE of FAMA-based perovskite devices. Upon incorporating 1H-CBH, the PCE is enhanced from 21.18% to 23.59%, driven by a notable increase in the V_{oc} from 1.15 V to 1.18 V, accompanied by significantly improved device reproducibility. Notable stability improvements are achieved through 1H-CBH passivation. The unencapsulated PSCs retain over 80% of their initial PCE after 600 h of storage under nitrogen atmosphere, whereas the control devices lose 20% of their efficiency within 150 h. This study introduces a transformative approach to additive engineering in PSCs, showing that rationally designed molecules capable of forming both coordination and hydrogen bonds can simultaneously constrain multiple degradation pathways. The multi-passivation strategy effectively mitigates ion migration, phase segregation, and crystallinity degradation, thereby enhancing both the photovoltaic efficiency and operational stability of the resulting devices. By incorporating 1H-CBH, we achieve a critical balance between high performance and long-term durability, advancing the commercial viability of perovskite solar technology.

Acknowledgements

None.

Author contribution statement

Guodan Wei and Chengcheng Wu conceived and designed the research, and supervised the project. Zhuo Peng and Han Wang carried out the experiments, fabricated perovskite solar cells, and conducted key characterization, drafting the initial manuscript. Jiazhi Meng, Xin Hong, Kefei Shi, Wenqiang Ding, Jianghao Yin and Na Liu provided critical analysis and feedback. Feiyu Kang and Guodan Wei secured funding and managed administrative tasks. All the authors have reviewed and aproved the final manuscript.

Data availability

The data that support the findings of this study are available from the corresponding authors upon reasonable request.

Declaration of competing interest

Feiyu Kang is the Editor-in-Chief of this journal, but he was not involved in the peer-review or decision-making of this article. All the other contributing authors report no conflicts of interest in this work.

Funding

The authors thank the support of the National Natural Science Foundation of China (Grant No. 52027817), the Shenzhen Distinguished Talent Program (Grant No. 01090100002), and the Tsinghua Shenzhen International Graduate School Overseas Research Cooperation Fund (Grant No. HW2024008).

Use of AI statement

None.

Electronic Supplementary Material: Further details of GIWAXS characterization, UPS spectra, Tauc plots, energy level diagram, time-dependent XRD measurements are available in the online version of this article at https://doi.org/10.26599/EMD.2026.9370088

References

[1] Wojciechowski, K., Forgács, D. (2022). Commercial applications of indoor photovoltaics based on flexible perovskite solar cells. *ACS Energy Lett.* 7, 3729–3733.

[2] Ling, J. K., Kizhakkedath, P. K. K., Watson, T. M., Mora-Seró, I., Schmidt-Mende, L., Brown, T. M., Jose, R. (2021). A perspective on the commercial viability of perovskite solar cells. *Sol. RRL* 5, 2100401.

[3] Mcgovern, L., Alarcón-Lladó, E., Garnett, E. C., Ehrler, B., van der Zwaan, B. (2023). Perovskite solar modules for the residential sector. *ACS Energy Lett.* 8, 4862–4866.

[4] Pearce, P. M., Halme, J., Jiang, J. Y., Ekins-Daukes, N. J. (2024). Efficiency limits and design principles for multi-junction coloured photovoltaics. *Energy Environ. Sci.* 17, 1189–1201.

[5] Green, M., Dunlop, E., Yoshita, M., Kopidakis, N., Bothe, K., Siefer, G., Hao, X. J., Jiang, J. Y. (2025). Solar cell efficiency tables (version 66). *Prog. Photovolt.: Res. Appl.* 33, 795–810.

[6] Shockley, W., Queisser, H. J. (1961). Detailed balance limit of efficiency of *p*-*n* junction solar cells. *J. Appl. Phys.* 32, 510–519.

[7] Hang, P. J., Kan, C. X., Li, B., Yao, Y. X., Hu, Z. C., Zhang, Y. Q., Xie, J. S., Wang, Y., Yang, D. R., Yu, X. G. (2023). Highly efficient and stable wide-bandgap perovskite solar cells via strain management. *Adv. Funct. Mater.* 33, 2214381.

[8] Wang, X. T., Chen, Y. T., Zhang, T. Y., Wang, Y., Kan, M., Miao, Y. F., Chen, H. R., Liu, X. M., Shi, J. L., Zhao, Y. X. (2020). Intrinsically stable wide band gap Br-free $Cs_xFA_{1-x}PbI_3$ (x= 0.5–0.9) perovskites overcoming phase segregation. *ChemRxiv*. chemrxiv.13048490.v1.

[9] Wang, X. T., Chen, Y. T., Zhang, T. Y., Wang, X. Y., Wang, Y., Kan, M., Miao, Y. F., Chen, H. R., Liu, X. M., Wang, X. J. et al. (2021). Stable cesium-rich formamidinium/cesium pure-iodide perovskites for efficient photovoltaics. *ACS Energy Lett.* 6, 2735–2741.

[10] Song, Z. L., Yang, J., Dong, X. Y., Wang, R., Dong, Y. X., Liu, D. X., Liu, Y. S. (2023). Inverted wide-bandgap 2D/3D perovskite solar cells with >22% efficiency and low voltage loss. *Nano Lett.* 23, 6705–6712.

[11] Zhang, X. P., Li, X. Y., Tao, L., Zhang, Z. M., Ling, H., Fu, X., Wang, S. B., Ko, M. J., Luo, J. S., Chen, J. Z. et al. (2023). Precise control of crystallization and phase-transition with green anti-solvent in wide-bandgap perovskite solar cells with open-circuit voltage exceeding 1.25 V. *Small* 19, 2208289.

[12] Yang, G., Ni, Z. Y., Yu, Z. J., Larson, B. W., Yu, Z. H., Chen, B., Alasfour, A., Xiao, X., Luther, J. M., Holman, Z. C. et al. (2022). Defect engineering in wide-bandgap perovskites for efficient perovskite–silicon tandem solar cells. *Nat. Photon.* 16, 588–594.

[13] Liu, Z., Zhu, C. H., Luo, H. W., Kong, W. C., Luo, X., Wu, J. L., Ding, C. Z., Chen, Y. Y., Wang, Y. R., Wen, J. et al. (2023). Grain regrowth and bifacial passivation for high-efficiency wide-bandgap perovskite solar cells. *Adv. Energy Mater.* 13, 2203230.

[14] Hassan, A., Wang, Z. J., Ahn, Y. H., Azam, M., Khan, A. A., Farooq, U., Zubair, M., Cao, Y. (2022). Recent defect passivation drifts and role of additive engineering in perovskite photovoltaics. *Nano Energy* 101, 107579.

[15] Dunfield, S. P., Bliss, L., Zhang, F., Luther, J. M., Zhu, K., van Hest, M. F. A.M., Reese, M. O., Berry, J. J. (2020). From defects to degradation: a mechanistic understanding of degradation in perovskite solar cell devices and modules. *Adv. Energy Mater.* 10, 1904054.

[16] Ono, L. K., Liu, S. Z., Qi, Y. B. (2020). Reducing detrimental defects for high-performance metal halide perovskite solar cells. *Angew. Chem. Int. Ed.* 59, 6676–6698.

[17] Dong, Q. S., Zhu, C., Chen, M., Jiang, C., Guo, J. Y., Feng, Y. L., Dai, Z. H., Yadavalli, S. K., Hu, M. Y., Cao, X. et al. (2021). Interpenetrating interfaces for efficient perovskite solar cells with high operational stability and mechanical robustness. *Nat. Commun.* 12, 973.

[18] Zheng, X. T., Kong, W. C., Wen, J., Hong, J. J., Luo, H. W., Xia, R., Huang, Z. L., Luo, X., Liu, Z., Li, H. J. et al. (2024). Solvent engineering for scalable fabrication of perovskite/silicon tandem solar cells in air. *Nat. Commun.* 15, 4907.

[19] Siekmann, J., Ravishankar, S., Kirchartz, T. (2021). Apparent defect densities in halide perovskite thin films and single crystals. *ACS Energy Lett.* 6, 3244–3251.

[20] Ni, Z. Y., Bao, C. X., Liu, Y., Jiang, Q., Wu, W. Q., Chen, S. S., Dai, X. Z., Chen, B., Hartweg, B., Yu, Z. S. et al. (2020). Resolving spatial and energetic distributions of trap states in metal halide perovskite solar cells. *Science* 367, 1352–1358.

[21] Abbas, M., Xu, X. W., Rauf, M., Kyaw, A. K. K. (2024). A comprehensive review on defects-induced voltage losses and strategies toward highly efficient and stable perovskite solar cells. *Photonics* 11, 87.

[22] Warby, J., Shah, S., Thiesbrummel, J., Gutierrez-Partida, E., Lai, H. G., Alebachew, B., Grischek, M., Yang, F. J., Lang, F., Albrecht, S. et al. (2023). Mismatch of quasi-Fermi level splitting and V_{oc} in perovskite solar cells. *Adv. Energy Mater.* 13, 2303135.

[23] Cacovich, S., Vidon, G., Degani, M., Legrand, M., Gouda, L., Puel, J. B., Vaynzof, Y., Guillemoles, J. F., Ory, D., Grancini, G. (2022). Imaging and quantifying non-radiative losses at 23% efficient inverted perovskite solar cells interfaces. *Nat. Commun.* 13, 2868.

[24] Remmerswaal, W. H. M., Van Gorkom, B. T., Zhang, D., Wienk, M. M., Janssen, R. A. J. (2024). Quantifying non-radiative recombination in passivated wide-bandgap metal halide perovskites using absolute photoluminescence spectroscopy. *Adv. Energy Mater.* 14, 2303664.

[25] Huang, H. H., Yang, T. A., Su, L. Y., Chen, C. H., Chen, Y. T., Ghosh, D., Lin, K. F., Tretiak, S., Chueh, C. C., Nie, W. Y. et al. (2023). Thiophene-based polyelectrolyte boosts high-performance

quasi-2D perovskite solar cells with ultralow energy loss. *ACS Mater. Lett.* 5, 1384–1394.

[26] Sun, Y. S., Ji, S., Yu, C. J., Liu, W. F., Wang, K. X., Huo, X. N., Sun, W. W., Yin, R., You, T. T., Yin, P. G. (2023). Regulation of phase arrangement in 2D ruddlesden-popper perovskite films via anti-solvent method for efficient solar cells. *Sol. Energy Mater. Sol. Cells* 262, 112568.

[27] Wang, H., Chan, C. C. S., Chu, M., Xie, J. S., Zhao, S. H., Guo, X. L., Miao, Q., Wong, K. S., Yan, K. Y., Xu, J. B. (2020). Interlayer cross-linked 2D perovskite solar cell with uniform phase distribution and increased exciton coupling. *Sol. RRL* 4, 1900578.

[28] Sun, A. X., Tian, C. C., Zhuang, R. S., Chen, C., Zheng, Y. T., Wu, X. Y., Tang, C., Liu, Y., Li, Z. H., Ouyang, B. L. et al. (2024). High open-circuit voltage (1.197 V) in large-area (1 cm^2) inverted perovskite solar cell via interface planarization and highly polar self-assembled monolayer. *Adv. Energy Mater.* 14, 2303941.

[29] Wang, H. Y., Xu, H. J., Wu, S. H., Wang, Y., Wang, Y., Wang, X. H., Liu, X. D., Huang, P. (2023). Synergistic lattice regulation of additive and interface engineering to realize high efficiency $CsPbI_2Br$ perovskite solar cell. *Chem. Eng. J.* 476, 146587.

[30] Wang, H. Y., Wang, Z., Tang, X. Y., Liu, L., Zhang, H. L., Yao, X. H., Wang, F. R., Wu, S. H., Liu, X. D. (2023). Understanding the doping effect in $CsPbI_2Br$ solar cells: crystallization kinetics, defect passivation and energy level alignment. *Chem. Eng. J.* 453, 139952.

[31] Patil, J. V., Mali, S. S., Park, D. W., Hong, C. K. (2021). Novel ytterbium-doped $CsPbI_2Br$ thin-films-based inorganic perovskite solar cells toward improved phase stability. *Mater. Today Chem.* 22, 100557.

[32] Jeong, M. J., Jeon, S. W., Kim, S. Y., Noh, J. H. (2023). High fill factor $CsPbI_2Br$ perovskite solar cells via crystallization management. *Adv. Energy Mater.* 13, 2300698.

[33] Saykar, N. G., Iqbal, M., Pawar, M., Chavan, K. T., Mahapatra, S. K. (2022). Dual-functional 3-acetyl-2,5-dimethylthiophene additive-assisted crystallization control and trap state passivation for high-performance perovskite solar cells. *ACS Appl. Energy Mater.* 5, 14701–14711.

[34] Lee, J. W., Tan, S., Seok, S. I., Yang, Y., Park, N. G. (2022). Rethinking the A cation in halide perovskites. *Science* 375, eabj1186.

[35] Liang, J. W., Hu, X. Z., Wang, C., Liang, C., Chen, C., Xiao, M., Li, J. S., Tao, C., Xing, G. C., Yu, R. et al. (2022). Origins and influences of metallic lead in perovskite solar cells. *Joule* 6, 816–833.

[36] Kamat, P. V., Kuno, M. (2021). Halide ion migration in perovskite nanocrystals and nanostructures. *Acc. Chem. Res.* 54, 520–531.

[37] Huang, X. F., Wu, B. H., Zheng, N. F. (2025). Optimizing solvent chemistry for high-quality halide perovskite films. *Acc. Mater. Res.* 6, 40–51.

[38] Xiang, W. C., Zhang, J. H., Liu, S. Z., Albrecht, S., Hagfeldt, A., Wang, Z. W. (2022). Intermediate phase engineering of halide perovskites for photovoltaics. *Joule* 6, 315–339.

[39] Rizzo, A., Listorti, A., Colella, S. (2022). Chemical insights into perovskite ink stability. *Chem* 8, 31–45.

[40] Wu, X., Zhang, L., Xu, Z., Olthof, S., Ren, X. D., Liu, Y. C., Yang, D., Gao, F., Liu, S. Z. (2020). Efficient perovskite solar cells *via* surface passivation by a multifunctional small organic ionic compound. *J. Mater. Chem. A* 8, 8313–8322.

[41] Xie, L. S., Liu, J., Li, J., Liu, C., Pu, Z. W., Xu, P., Wang, Y. H., Meng, Y. Y., Yang, M. J., Ge, Z. Y. (2023). A deformable additive on defects passivation and phase segregation inhibition enables the efficiency of inverted perovskite solar cells over 24%. *Adv. Mater.* 35, 2302752.

[42] Byranvand, M. M., Saliba, M. (2021). Defect passivation of perovskite films for highly efficient and stable solar cells. *Sol. RRL* 5, 2100295.

[43] Pereyra, C., Xie, H. B., Lira-Cantu, M. (2021). Additive engineering for stable halide perovskite solar cells. *J. Energy Chem.* 60, 599–634.

[44] Mahdi, Z. H., Alsalim, T. A., Abdulhussein, H. A., Majed, A. A., Abbas, S. (2024). Synthesis, molecular docking, and anti-breast cancer study of 1-H-indol-3-Carbohydrazide and their derivatives. *Results Chem.* 11, 101762.

[45] Ma, Z., Zhou, W. Y., Huang, D. J., Liu, Q. Y., Xiao, Z., Jiang, H. F., Yang, Z. Q., Zhang, W. F., Huang, Y. L. (2020). Nicotinamide as additive for microcrystalline and defect passivated perovskite solar cells with 21.7% efficiency. *ACS Appl. Mater. Interfaces* 12, 52500–52508.

[46] Hung, C. M., Lin, J. T., Yang, Y. H., Liu, Y. C., Gu, M. W., Chou, T. C., Wang, S. F., Chen, Z. Q., Wu, C. C., Chen, L. C. et al. (2022). Modulation of perovskite grain boundaries by electron donor-acceptor zwitterions *R,R*-diphenylamino-phenyl-pyridinium-$(CH_2)_n$-sulfonates: all-round improvement on the solar cell performance. *JACS Au* 2, 1189–1199.

[47] Park, B. W., Kwon, H. W., Lee, Y., Lee, D. Y., Kim, M. G., Kim, G., Kim, K. J., Kim, Y. K., Im, J., Shin, T. J. et al. (2021). Stabilization of formamidinium lead triiodide α-phase with isopropylammonium chloride for perovskite solar cells. *Nat. Energy* 6, 419–428.

[48] Yuan, G. Z., Xie, W. Q., Song, Q. Z., Ma, S., Ma, Y., Shi, C. B., Xiao, M. Q., Pei, F. T., Niu, X. X., Zhang, Y. et al. (2023). Inhibited crack development by compressive strain in perovskite solar cells with improved mechanical stability. *Adv. Mater.* 35, 2211257.

[49] Yang, T. H., Gao, L. L., Lu, J., Ma, C., Du, Y. C., Wang, P. J., Ding, Z. C., Wang, S. Q., Xu, P., Liu, D. L. et al. (2023). One-stone-for-two-birds strategy to attain beyond 25% perovskite solar cells. *Nat. Commun.* 14, 839.

[50] Zhu, L., Cao, H., Xue, C., Zhang, H., Qin, M. C., Wang, J., Wen, K. C., Fu, Z. W., Jiang, T., Xu, L. et al. (2021). Unveiling the additive-assisted oriented growth of perovskite crystallite for high performance light-emitting diodes. *Nat. Commun.* 12, 5081.

[51] Liang, Y. G., Chen, G. D., Wang, Y., Zou, Y., Feng, M. L., Wang, Y. M., Li, B. W., Cho, Y., Chang, Y. D., Liu, T. L. et al. (2025). A matrix-confined molecular layer for perovskite photovoltaic modules. *Nature* 648, 91–96.

[52] Patel, S. K., Nayak, S., Senanayak, S. P. (2023). Impact of B-Site cation substitution on ionic and electronic charge transport in metal halide perovskites. *ACS Appl. Electron. Mater.* 5, 5371–5377.

[53] Gao, Y., Xu, W. Z., Zhang, S. W., Fan, T. J., Zhang, M., Ran, A. H., Zhang, X., Kang, F. Y., Wei, G. D. (2022). Double cascading charge transfer at integrated perovskite/organic bulk heterojunctions for extended near-infrared photoresponse and enhanced photocurrent. *Small* 18, 2106083.

[54] Degani, M., An, Q. Z., Albaladejo-Siguan, M., Hofstetter, Y. J., Cho, C., Paulus, F., Grancini, G., Vaynzof, Y. (2021). 23.7% efficient inverted perovskite solar cells by dual interfacial modification. *Sci. Adv.* 7, eabj7930.

[55] Meng, J. Z., Gao, Y., Hu, J. N., Wu, C. C., Li, Y., Zhang, S. W., Chen, Y. Q., Kerner, R. A., Ma, J., Shen, Y. et al. (2025). Deuterium-substituted cations enhance perovskite solar cell efficiency and stability. *Joule* 9, 102031.

[56] Cheng, W. J., He, X., Wang, J. G., Tian, W., Li, L. (2022). *N*-(2-aminoethyl) acetamide additive enables phase-pure and stable α-

$FAPbI_3$ for efficient self-powered photodetectors. *Adv. Mater.* 34, 2208325.

[57] Ollearo, R., Wang, J. K., Dyson, M. J., Weijtens, C. H. L., Fattori, M., Van Gorkom, B. T., Van Breemen, A. J. J. M., Meskers, S. C. J., Janssen, R. A. J., Gelinck, G. H. (2021). Ultralow dark current in near-infrared perovskite photodiodes by reducing charge injection and interfacial charge generation. *Nat. Commun.* 12, 7277.

[58] Wang, B., Li, H., Dai, Q. Q., Zhang, M., Zou, Z. G., Brédas, J. L., Lin, Z. Q. (2021). Robust molecular dipole-enabled defect passivation and control of energy-level alignment for high-efficiency perovskite solar cells. *Angew. Chem. Int. Ed.* 60, 17664–17670.

[59] Yang, I. S., Park, N. G. (2021). Dual additive for simultaneous improvement of photovoltaic performance and stability of perovskite solar cell. *Adv. Funct. Mater.* 31, 2100396.

[60] Jeon, N. J., Noh, J. H., Yang, W. S., Kim, Y. C., Ryu, S., Seo, J., Seok, S. I. (2015). Compositional engineering of perovskite materials for high-performance solar cells. *Nature* 517, 476–480.

[61] He, W., Yang, X. Y., Duan, J. L., Zhang, J. S., Guo, Q. Y., Huang, H., Tang, Q. W. (2023). Liquid buried interface to slide lattice and heal defects in inorganic perovskite solar cells. *J. Colloid Interface Sci.* 646, 695–702.

[62] Datta, K., Van Gorkom, B. T., Chen, Z. H., Dyson, M. J., van der Pol, T. P. A., Meskers, S. C. J., Tao, S. X., Bobbert, P. A., Wienk, M. M., Janssen, R. A. J. (2021). Effect of light-induced halide segregation on the performance of mixed-halide perovskite solar cells. *ACS Appl. Energy Mater.* 4, 6650–6658.